ADVANCED ELECTRONIC MATERIALS Open Access
www.advelectronicmat.de

Multilayer Metamaterials with Ferromagnetic Domains Separated by Antiferromagnetic Domain Walls

Ruslan Salikhov, Fabian Samad, Sebastian Schneider, Darius Pohl, Bernd Rellinghaus, Benny Böhm, Rico Ehrler, Jürgen Lindner, Nikolai S. Kiselev,* and Olav Hellwig**

In memory of Anthony Schuyler Arrott

Magnetic nano-objects possess great potential for more efficient data processing, storage, and neuromorphic-type applications. Using high perpendicular magnetic anisotropy synthetic antiferromagnets in the form of multilayer-based metamaterials, the antiferromagnetic interlayer exchange energy is purposefully reduced below the out-of-plane demagnetization energy, which controls magnetic domain formation. In this unusual magnetic energy regime, as demonstrated via macroscopic magnetometry and microscopic Lorentz transmission electron microscopy, it becomes possible to stabilize nanometer-scale stripe and bubble textures consisting of ferromagnetic out-of-plane domain cores separated by antiferromagnetic in-plane Bloch-type domain walls. This unique coexistence of mixed ferromagnetic/antiferromagnetic order on the nanometer scale opens so far unexplored perspectives in the architecture of magnetic domain landscapes as well as the design and functionality of individual magnetic textures, such as bubble domains with depth-wise alternating chirality.

1. Introduction

The engineering and control of the domain-wall (DW) spin structure in magnetic systems is a crucial area of research for magnetic logic and memory applications, as the dynamic properties of magnetic solitons or DWs themselves strongly depend on it. Additionally, it further impacts the response of DWs to external stimuli, such as magnetic fields and electric currents, and their interaction with other magnetic DWs.[1–11] In order to control the internal DW spin structure, it is attractive to use magnetic multilayer (ML) structures, where the respective magnetic energy terms can be adjusted by interfacing of different materials.[7–9] For example, the locking of DW chirality, leading to skyrmion-like magnetic textures, has been realized via the interfacial Dzyaloshinskii–Moriya interaction (IDMI).[1,12,13] Additionally, by exploiting the Ruderman–Kittel–Kasuya–Yoshida (RKKY) type interlayer exchange coupling,[14,15] domains and DWs that are antiferromagnetically (AF) coupled across a non-magnetic spacer layer have been realized in synthetic antiferromagnets (SAFs).[16–22] Both the AF-DWs[16] and skyrmion bubbles in SAFs[17] can be driven more efficiently by spin-orbit torques with much smaller current density than it is typically necessary for efficient DW movement in ferromagnetic (FM) MLs. This highlights the potential of SAFs as a promising platform for energy-efficient magnetic logic and memory devices.[23–25]

Unlike the direct exchange in intrinsic antiferromagnets, the interlayer exchange coupling (IEC) in SAFs (E_{IEC}) is much weaker

R. Salikhov, F. Samad, J. Lindner, O. Hellwig
Institute of Ion Beam Physics and Materials Research
Helmholtz-Zentrum Dresden-Rossendorf
Bautzner Landstraße 400, 01328 Dresden, Germany
E-mail: r.salikhov@hzdr.de; o.hellwig@hzdr.de

F. Samad, B. Böhm, R. Ehrler, O. Hellwig
Institute of Physics
Chemnitz University of Technology
Reichenhainer Straße 70, 09107 Chemnitz, Germany

F. Samad, B. Böhm, R. Ehrler, O. Hellwig
Center for Materials, Architectures and Integration of Nanomembranes (MAIN)
Chemnitz University of Technology
Rosenbergstraße 6, 09107 Chemnitz, Germany

S. Schneider, D. Pohl, B. Rellinghaus
Dresden Center for Nanoanalysis, cfaed
Technische Universität Dresden
01069 Dresden, Germany

N. S. Kiselev
Peter Grünberg Institute
Forschungszentrum Jülich and JARA
52425 Jülich, Germany
E-mail: n.kiselev@fz-juelich.de

The ORCID identification number(s) for the author(s) of this article can be found under https://doi.org/10.1002/aelm.202400251

DOI: 10.1002/aelm.202400251

and can be balanced with other magnetic energy terms, such as perpendicular magnetic anisotropy (PMA) (E_{PMA}) and magnetostatic dipole interaction (E_{demag}).[26–31] These terms shape the domain structure and DW spin configuration in magnetic MLs. The strength of the demagnetization energy in a uniformly magnetized ML system is highly dependent on the orientation of the magnetization with respect to the thin film geometry. When tuning the interlayer AF exchange coupling energy to be about equal to the out-of-plane demagnetization energy in a PMA-SAF system, both FM and AF phases can coexist.[26–29] Furthermore, even if the demagnetization energy leads to the formation of a regular periodic FM stripe domain pattern, locally hidden AF configurations will still exist within in-plane oriented regions, for example within the Bloch type DWs. This so far experimentally not demonstrated mixed FM domain core and AF domain wall structure originates from the unusual maximum energy configuration ($|E_{PMA}| > |E_{demag}| > |E_{IEC}| > 0$), which can be precisely controlled in the multilayer metamaterials that we employ here for its experimental implementation. In a typical stripe domain state of a PMA-FM system, the out-of-plane domain pattern is stabilized by the dipolar interaction between the nearest domain magnetic moments. Meanwhile, the in-plane DW Bloch components exhibit degeneracy in terms of magnetization direction and can even be manipulated using small in-plane magnetic fields.[32] In the PMA-SAF system, characterized by a periodic stripe domain structure dominated by demagnetization energy, even a weak AF interlayer exchange coupling aligns the DW Bloch components into a block-wise AF order. Consequently, the magnetic ground state of the PMA-SAF system comprises out-of-plane FM domain cores separated by in-plane AF Bloch-type DWs. Recent magnetic simulations, inspired by the experiments presented in this manuscript, have revealed that such DWs with alternating in-plane chirality in magnetic stripe and bubble domains can even be present in systems, where any IEC (FM or AF) is absent.[33] However, the reported wide diversity of FM and AF DW states, in this case, introduces additional complexity and thus unnecessary challenges to an experimental demonstration.[33]

In this work, we explore SAF systems using highly tunable, application-friendly ML structures of the type $\{[Co/Pt]_{X-1}/Co/Ru\}_{N-1}[Co/Pt]_X$, which possess strong PMA. We demonstrate that our PMA-SAF system exhibits FM behavior with stripe and bubble domains in the ground state, similar as observed for $[Co/Pt]_X$ reference samples. A detailed study of the magnetic field reversal behavior and the magnetic DW structure on the macro- (magnetometry) as well as on the micro-scale (Lorentz transmission electron microscopy), however, shows that in the PMA-SAFs the Bloch-type DWs possess an in-depth AF ordering. The observation of AF-DWs between FM domains is also consistent with the results of micromagnetic simulations. These results extend the spin configuration possibilities for magnetic solitons and provide a way to control and design the internal DW spin structure, which is a key ingredient that defines the dynamic limits for race-track-memory-type applications. Furthermore, such mixed FM/AF spin textures may extend the frequency range in DW-based magnonics[34–37] and the possible configurations in neuromorphic and reservoir computing type of applications.[24,38–42]

2. Results and Discussion

2.1. Macroscopic Magnetization Averaged Characterization

In order to demonstrate the key differences between PMA-SAFs and FM MLs with PMA, we fabricated two different sets of samples as schematically depicted in the inset of **Figure 1a**. The first set (we refer to as SAF) consists of $\{[Co(0.44\ nm)/Pt(0.7\ nm)]_{X-1}/Co(0.44\ nm)/Ru(0.9\ nm)\}_{N-1}[Co(0.44\ nm)/Pt(0.7\ nm)]_X$ with $(X, N) = (12, 4)$ (as well as (10,10)). The second set (we refer to as Co/Pt) consists of $[Co(0.44\ nm)/Pt(0.7\ nm)]_X$ PMA-MLs with $X = 48$ (as well as 100). The thicknesses of the Co and Pt layers (given in parentheses) were chosen to provide strong PMA (see the Experimental Section). The thickness of the Ru-layer was adjusted for the strongest AF coupling between the Co-layers, which has an oscillatory dependence on the Ru thickness due to the RKKY-type interaction.[14,15,43] The structural comparison of PMA-SAF and PMA-FM systems is provided in Figure S1 (Supporting Information).

The magnetic hysteresis loops of two samples, SAF $(X, N) = (12, 4)$ and Co/Pt $X = 48$ are compared in Figure 1a,b. The out-of-plane magnetization measurements (Figure 1a) reveal identical easy-axis behavior for both samples, indicating that the magnetization reversal mechanism via domain nucleation and annihilation is identical in both systems. Thus, the SAF sample exhibits PMA ferromagnetic characteristics as well. However, the in-plane magnetization measurements (Figure 1b), when carefully examined reveal a distinct difference at remanence (zero magnetic field). Specifically, the Co/Pt sample exhibits a non-zero remanent moment, while the SAF sample has almost no remanence as shown in the inset of Figure 1b. The nonzero remanent moment in Co/Pt is caused by the magnetization within Bloch-type DWs, which separate stripe domains formed at the magnetization reversal, as reported in Ref. [32]. Consequently, the vanishing remanence in the SAF system indicates the absence of net magnetization from the Bloch-type DWs. A similar behavior is observed when comparing the SAF $(X, N) = (10, 10)$ system with the respective Co/Pt $X = 100$ ML sample (see Figure S2, Supporting Information).

Owing to the fact that the remanent in-plane magnetization originates from the Bloch-type DW polarization, one can study the characteristics of the DW magnetic switching using magnetometry.[32] To stabilize the aligned stripe-domain state in all samples, an in-plane ac-demagnetization (ACD) protocol is employed (details can be found in the Experimental Section). After ACD, both systems exhibit parallel stripe domains aligned along the direction of the ACD magnetic field, as evidenced by the magnetic force microscopy (MFM) images in the corresponding insets in Figure 1c,d. The domain period of both samples is identical and estimated to be 160 ± 10 nm. Next, we performed a series of minor-loop measurements for SAF (Figure 1c) and Co/Pt (Figure 1d) samples symmetrically around remanence with the magnetic field applied parallel to the stripe-domain's long axis in order to track the field-dependent DW-magnetization behavior. All minor hysteresis loops for the Co/Pt ML, for fields above 50 mT, are hysteretic (Figure 1d) with an opening between the ascending and descending branches and an increase

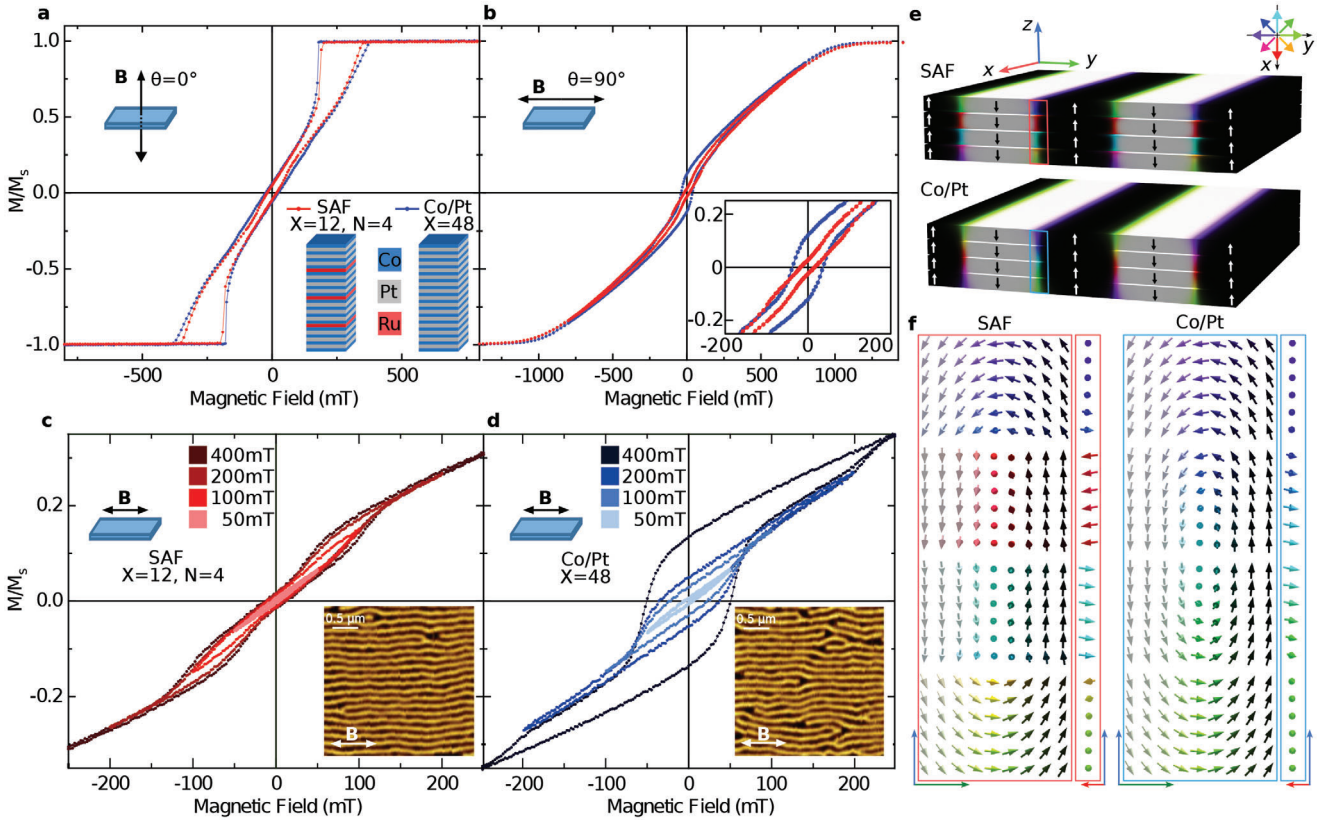

Figure 1. Comparison of magnetic states in PMA-SAFs and PMA-FM systems. a,b) Comparison of magnetic hysteresis loops recorded in out-of-plane a) and in-plane b) geometry for $[[Co(0.44\ nm)/Pt(0.7\ nm)]_{11}/Co(0.44\ nm)/Ru(0.9\ nm)]_3[Co(0.44\ nm)/Pt(0.7\ nm)]_{12}$ PMA-SAF and $[Co(0.44\ nm)/Pt(0.7\ nm)]_{48}$ PMA-FM MLs. While the out-of-plane loops show identical behavior, the in-plane loops exhibit different remanent magnetization, as is better seen in the enlarged view in the inset in (b). c,d) In-plane minor-loop series with the maximum magnetic field varied between 50 and 400 mT for c) PMA-SAF and d) PMA-FM systems. The field is applied parallel to the long axis of the stripe domains, as indicated in the MFM images shown in the corresponding insets. e) shows the results of micromagnetic simulations for the SAF ML (top) and FM ML (bottom). Colors encode the direction of magnetization according to a standard scheme: black and white denote up and down spins, respectively, and red-green-blue reflect the direction of the in-plane magnetization component, as shown in the top inset. (f) is the zoomed view into the domain walls between up and down domains in SAF ML (left) and FM ML (right). Note that the spacing of the Co/Pt blocks in the PMA-FM sample has been included to improve visualization and comparability, even though we use here a regular Pt(0.7 nm) interlayer instead of a Ru interlayer.

in remanent magnetization when the maximal magnetic field is increased. This behavior is attributed to the DW magnetization switching characteristics, which are explained in more detail in Ref. [32]. In contrast, the SAF system demonstrates almost linear and reversible behavior in response to the applied magnetic field (Figure 1c), with residual magnetization approaching zero, irrespective of the maximum field strength. This is a typical characteristic of AF-coupled magnetization. A slight opening at larger magnetic fields can be attributed to surface pinning of the DW magnetization at the upper and lower Co/Pt capping blocks in the SAF sample. This opening becomes negligible in a thicker SAF system with $(X, N) = (10, 10)$, where the cap volume constitutes a smaller fraction, as evident in Figure S2c (Supporting Information).

At this point, we shall exclude the contribution of IDMI, which could potentially lead to different in-plane magnetization behavior in SAFs and Co/Pt systems (see Figure 1c,d; Figure S2c,d, Supporting Information). Considering that both FM and AF MLs predominantly consist of Co/Pt interfaces grown under identical conditions, any contribution stemming from Co/Pt interface interdiffusion[44] or strain modulation[45] can be readily ruled out. Indeed, in the symmetric Pt/Co/Pt system, the DMI is negligible.[45] Given that in our SAF system, there are only a few Co layers with asymmetric Pt/Co/Ru interfaces (for the SAF $(X, N) = (12, 4)$, the ratio is 6/48), any significant contribution of the IDMI at Co/Ru interfaces can also be excluded. To verify this also experimentally, we fabricated two MLs, where the Ru-spacer layer was adjusted to two distinct thicknesses: 1.3 and 1.9 nm. At 1.3 nm, the RKKY interaction results in FM coupling between the Co layers, while at 1.9 nm, the coupling is AF.[14] The comparison of magnetic hysteresis loops from these samples with different Ru layer thicknesses is shown in Figure S3 (Supporting Information). When the Ru thickness is 1.3 nm, where the coupling is FM, the in-plane hysteresis loop exhibits similar characteristics to that of the Co/Pt ML with non-zero remanent magnetization. However, when we increase the Ru thickness to 1.9 nm, corresponding to the second maximum of the AF-coupling energy, the sample shows a vanishing remanent magnetization, similar to the SAF with 0.9 nm Ru. As the IDMI is not expected to depend on

the Ru thickness in an oscillatory manner, we can exclude its contribution to the DW magnetization behavior. At the same time, this provides clear evidence that the AF-like DW behavior is caused by the AF interlayer exchange coupling and is not caused by any other interfacial effects.

To confirm the DW spin structure in the SAF system, we employed micromagnetic simulations using Mumax[46] and Excalibur.[47] The details of the micromagnetic simulations are provided in the Experimental Section. The results of the numerical simulations for the SAF and Co/Pt systems are presented in Figure 1e, along with a magnification of the DWs between "up" and "down" domains in Figure 1f. Both systems exhibit an identical stripe-domain state, which is in line with the MFM data. On the other hand, the simulated DW spin structures of the two systems are very different. At the film surfaces both, SAF and Co/Pt systems display flux closing Néel-type DW components. In the center of the DWs, the Co/Pt system has an FM Bloch-type component which contributes an in-plane net magnetization to the DW. For the SAF system, the middle of the DW exhibits a subunit-wise in-plane AF ordering of magnetic moments with zero net magnetization. This explains the absence of a net magnetization in the in-plane major and minor loop magnetometry measurements in Figure 1b,c.

2.2. Microscopic Magnetic Characterization with Lorentz TEM

To reveal the presence of AF ordering not only by magnetization averaged measurements but also directly and spatially resolved within individual microscopic DWs, we designed a dedicated experiment using Lorentz transmission electron microscopy (LTEM). The LTEM measurements are typically conducted on respective sister samples that are deposited onto silicon nitride (Si_3N_4) membrane substrates. Due to internal mechanical strain between the Si_3N_4 and the metallic MLs these membrane samples usually exhibit buckled profiles with extensive folds and bends that form a characteristic stress pattern[48] as shown in **Figure 2**a,b. In many cases, this aspect is unfavorable to LTEM imaging, but we use it here specifically to our advantage. Given that LTEM is sensitive only to the net component of the magnetic induction perpendicular to the electron beam the contrast near the folded areas allows us to obtain unique information on different components of the magnetic induction of the sample in one and the same image (Figure 2c–f). Figure 2g illustrates the expected LTEM contrast of an isolated stripe domain passing across the fold line in the case of SAF and FM samples. When the electron beam is perpendicular to the membrane surface on top of a fold line, no LTEM contrast from the DWs in the SAF with compensated magnetic moments is detectable (see top row in Figure 2g). That is because LTEM is sensitive only to the net in-plane components of the magnetic induction. On the other hand, the projected in-plane magnetization of the DWs in the Co/Pt MLs results in a pronounced contrast that is consistently present for all angles of the electron beam to the sample normal, also at the top of a fold line, where the beam enters parallel to the surface normal (see the second and third rows in Figure 2g). Furthermore, the contrast of DWs in Co/Pt multilayers is expected to depend on the polarization direction of the adjacent DWs, as reported in Ref. [32].

When a TEM membrane is folded up and down (Figure 2a,b) due to the buckling effect, and the electron beam is adjusted to be parallel to the *z*-axis (Figure 2c,d), one obtains signals from the tilted "up" and "down" domain magnetizations wherever the local angle between the electron beam and domain magnetization deviates from zero. Since the tilt of the ML film is opposite for sections of the stripe domains on either side of the folding line (i.e., for opposite signs of the slope), the tilt-induced x-y-plane components of the domain magnetization have opposite directions. As a consequence, the magnetic contrast of the domains is expected to be inverted across the fold line along which the slope is zero. For zero slope there is no contrast from the perpendicular domain cores left, here along the fold lines only the DWs contribute to the LTEM contrast. Therefore, the inversion behavior of the magnetic contrast is expected to be different close to the fold line, depending on the DW spin configuration. According to our simulations, in the case of an AF spin structure, the inversion occurs through zero contrast at the fold line, since the AF-DWs have zero net magnetization (see the first row in Figure 2g,h). However, the magnetic contrast from the FM-DWs in Co/Pt MLs contributes to the LTEM signal across the folding line, resulting in a smooth transition with non-zero contrast, as seen in the second and third rows in Figure 2g,h.

By selecting different folding line areas for LTEM imaging (some examples are marked with black rectangles in Figure 2b), we were able to obtain representative experimental images of aligned stripe domain states in the SAF and Co/Pt samples, as seen in **Figure 3**a,d respectively. Figure 3b,c shows a magnification of selected areas in Figure 3a,d. Even at large fields of view in Figure 3a,d it becomes apparent that there is a significant difference in the LTEM contrasts between the two FM-domain states. The SAF sample shows no contrast at the fold line (which can be identified from the in-focus TEM image in the inset of Figure 3a), while the Co/Pt sample provides magnetic contrast everywhere in the studied area, even at normal electron incidence. This is due to the overlap of signals from the stripe domains in the tilted region with the signal from the Bloch-type DWs.

To isolate the magnetic signal from a single stripe domain, we apply an external magnetic field of ≈270–320 mT parallel to the electron beam direction. This causes the "up"-domains to grow and the "down"-domains to shrink. Figure 3e,h shows the corresponding under-focus LTEM images for SAF and Co/Pt samples. The over-focus LTEM images are shown in Figure S4 (Supporting Information) and compared with the corresponding under-focus images. Now it becomes apparent that all stripe domains invert the magnetic contrast in the two tilted regions across the folding line, see also the magnified area images in Figure 3f,g. Unlike the Co/Pt sample, which shows a continuous transition due to an additional contribution from Bloch-type DWs, the SAF sample displays no magnetic contrast along the folding line (where the electron beam transmits the sample at normal incidence). The observed behavior of the PMA-SAF sample in the LTEM images confirms on a local level for individual stripe domains the coexistence of mixed FM domain core and AF DW magnetic spin structures and is consistent with our earlier interpretation based on the magnetization averaged minor loop studies.

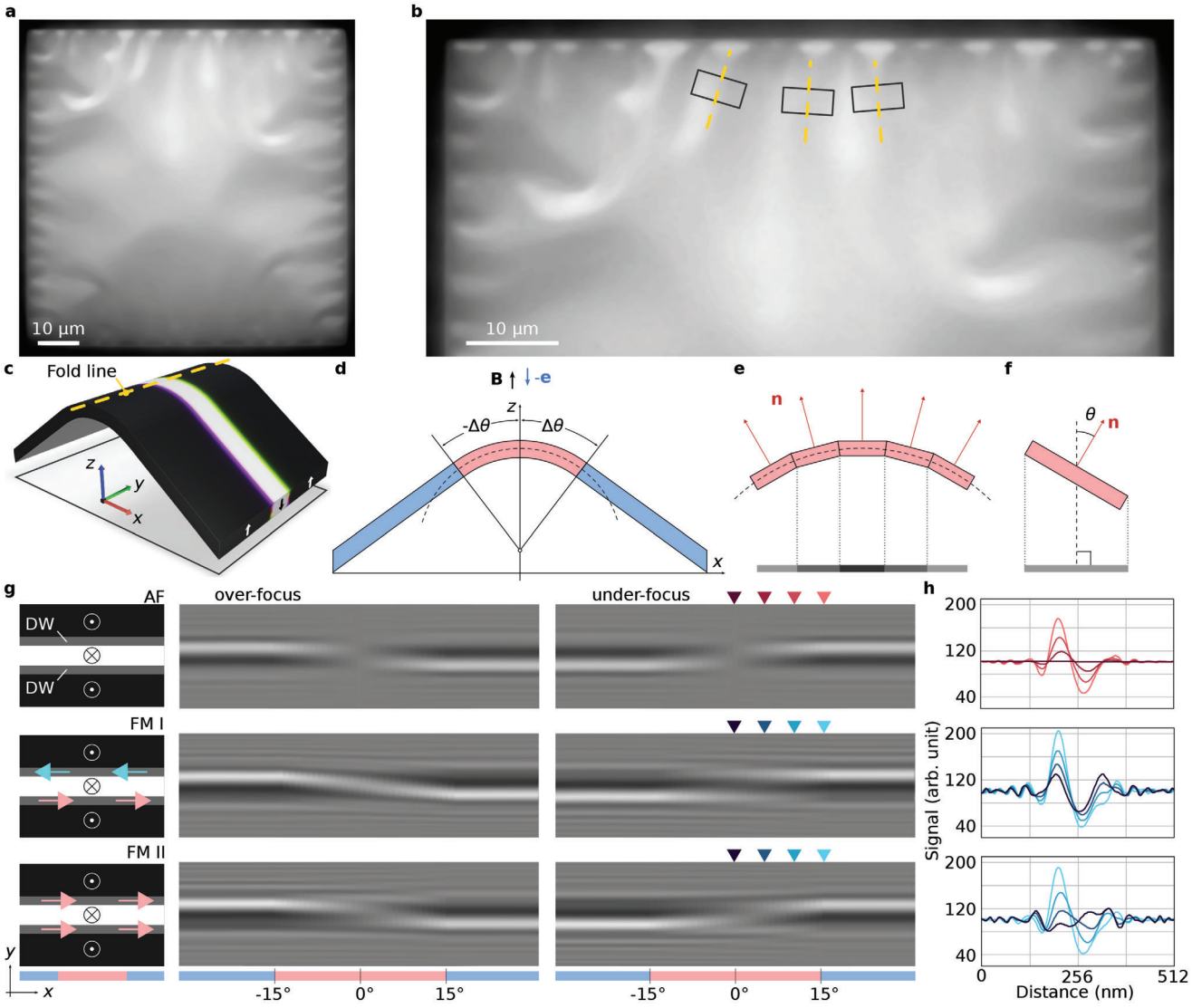

Figure 2. Theoretical LTEM images of isolated stripe domains in PMA-SAF and PMA-FM in the presence of surface folds. a) Representative example of an experimental in-focus TEM image of a ML sample on the Si_3N_4 membrane acquired at low magnification, (b) is a magnified area of (a). Some regions with folds appearing due to the buckling of the membrane are marked by black rectangles. The folding lines are marked by (yellow) dashed lines. c) Schematic illustration of a folding line (buckle) in a ML membrane film approximated by a circular arc segment and two flat segments tangential to it. In (d), the circular and flat segments are marked with red and blue, respectively. e) shows that the arc segment can be effectively approximated by an array of straight segments. As depicted in (f), the normal of each straight segment, n, has a certain well-defined tilt angle θ to the directions of the incident electron beam [blue arrow in (d)] and external magnetic field [black arrow in (d)]. g) shows theoretical over-focus and under-focus LTEM images of an isolated stripe domain passing perpendicular through the fold line as illustrated in (c). The top row corresponds to the stripe domains in an SAF, and the two rows below to the stripe domain in a FM Co/Pt ML, with two possible domain wall polarisations, as schematically illustrated in the first column. The complete images were obtained by placing together the images calculated for flat segments (512 × 512 nm) with tilt angle θ varying between −15° and +15° in steps of 1°. The images were calculated for a defocus of 2.8 mm. The plots in (h) show the cross-section profiles of under-focus images in (g). The positions of the cross-sections are marked in (g) by triangles of the corresponding color.

2.3. Extension from Parallel Stripe to Dense Bubble Domain States

Finally, we extend our study to FM bubble domains in SAFs that exhibit AF ordering within their DWs. By using the approach outlined in our previous study,[49] we stabilized dense bubble states in the (X, N) = (10, 10) SAF sample as well as in the Co/Pt sample with X = 100. Corresponding MFM images for the SAF and Co/Pt samples are presented in the respective insets in **Figure** 4a,b. Without altering the morphology of the bubble state we then measured minor hysteresis loop series (below 300 mT field), similar to those previously performed on the aligned stripe-domain state (see Figure S2c,d, Supporting Information). The results of these measurements for bubble states can be found in Figure 4a for the SAF sample and Figure 4b for the Co/Pt reference sample. Again, the Co/Pt sample shows irreversible switching

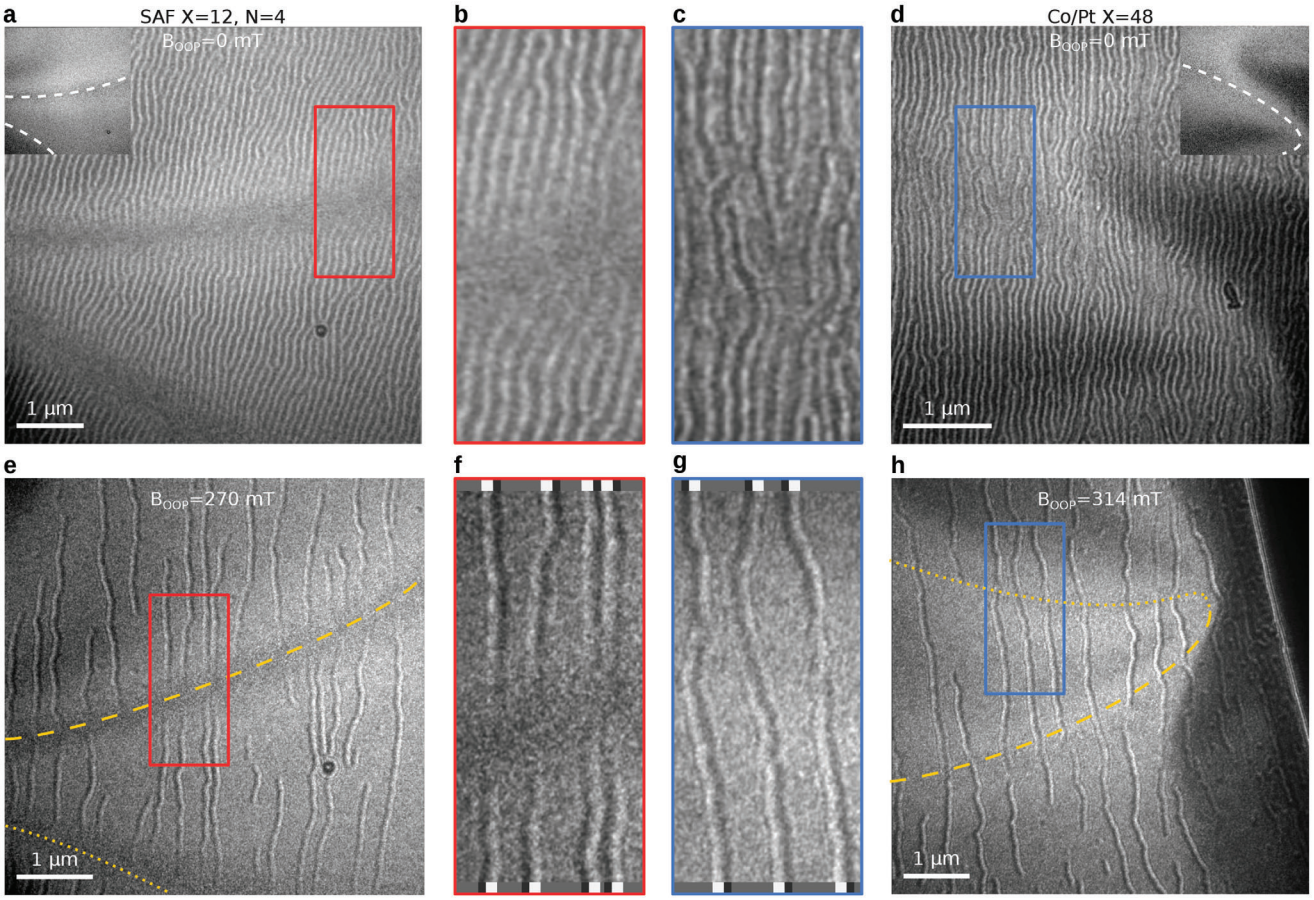

Figure 3. Direct evidence for the AF-DW states in SAFs using LTEM in Fresnel configuration. a–d) Under-focus LTEM images of aligned stripe-domain states in a) SAF and d) Co/Pt MLs. (b) and (c) are magnified areas marked with red and blue rectangles in (a) and (d), respectively. The images are taken at a defocus of 2 mm and zero external magnetic field. The insets in (a) and (d) show in-focus TEM images of the same area where the fold lines are marked by white dashed lines. (a) and (b) illustrate that in the case of SAF, the LTEM contrast of stripe domains completely vanishes at the fold lines. In the case of the Co/Pt multilayer in (c) and (d), the stripe domains exhibit high contrast, even when crossing the folding line. The diverse contrast patterns in (d) are because the DWs in Co/Pt sample are polarized in different directions. In the case of the SAF, in (a), the DWs have zero net magnetization and provide identical contrast patterns. (e) and (h) show the LTEM images (at a defocus of 2.8 mm) of isolated stripe domains at a high external magnetic field applied parallel to the e-beam direction in SAF and Co/Pt ML, respectively. The dashed yellow lines represent a valley in the buckled membrane, while dotted yellow lines mark the peak region. (f) and (g) are magnified areas marked with red and blue rectangles in (e) and (h), respectively. (f) and (g) show an inversion of the contrast of an individual stripe when crossing the fold line. Note that in (f), the contrast completely vanishes at the fold line.

of the DWs from one type-II state to another with opposite polarization via type-I states with different chiralities.[50,51] The magnetization of the DWs in the SAF sample shows almost fully reversible behavior, akin to antiferromagnets with a linear dependence on the applied field. This behavior is similar to what we previously observed in the aligned stripe-domain state of the same SAF sample with (X, N) = (10, 10) (see Figure S2c, Supporting Information), indicating that the magnetic bubbles in the PMA-SAF are of type-I, with alternating chirality across the Ru-layers. The latter finding agrees with the results of micromagnetic simulations for the SAF sample in Figure 4c, where we also observe the spontaneous formation of alternating chirality in adjacent AF sub-units within the domain walls of the bubble domains.

As seen in Figure 4c, the domain walls at the topmost and bottommost layers are shifted with respect to the domain walls in the internal layers. This phenomenon, known as the exchange shift of domain walls, has been studied in the literature earlier.[52,53] The exchange shift causes the magnetization in adjacent layers to be ordered antiferromagnetically with respect to each other. In the case of antiferromagnetic IEC, such ordering provides an extra energy gain in the narrow region between the shifted domain walls. Figure S5 (Supporting Information) provides some details about the challenges of imaging the bubble domain state using LTEM.

3. Conclusion

Our study reveals the presence of mixed FM/AF textures in SAF MLs with weak RKKY-type interlayer exchange coupling, which is overcome by the strong demagnetization fields within the perpendicular domain cores, but still prevails within the Bloch-type in-plane magnetized domain walls. As a result, we obtain so far unexplored types of mixed FM/AF textures featuring FM

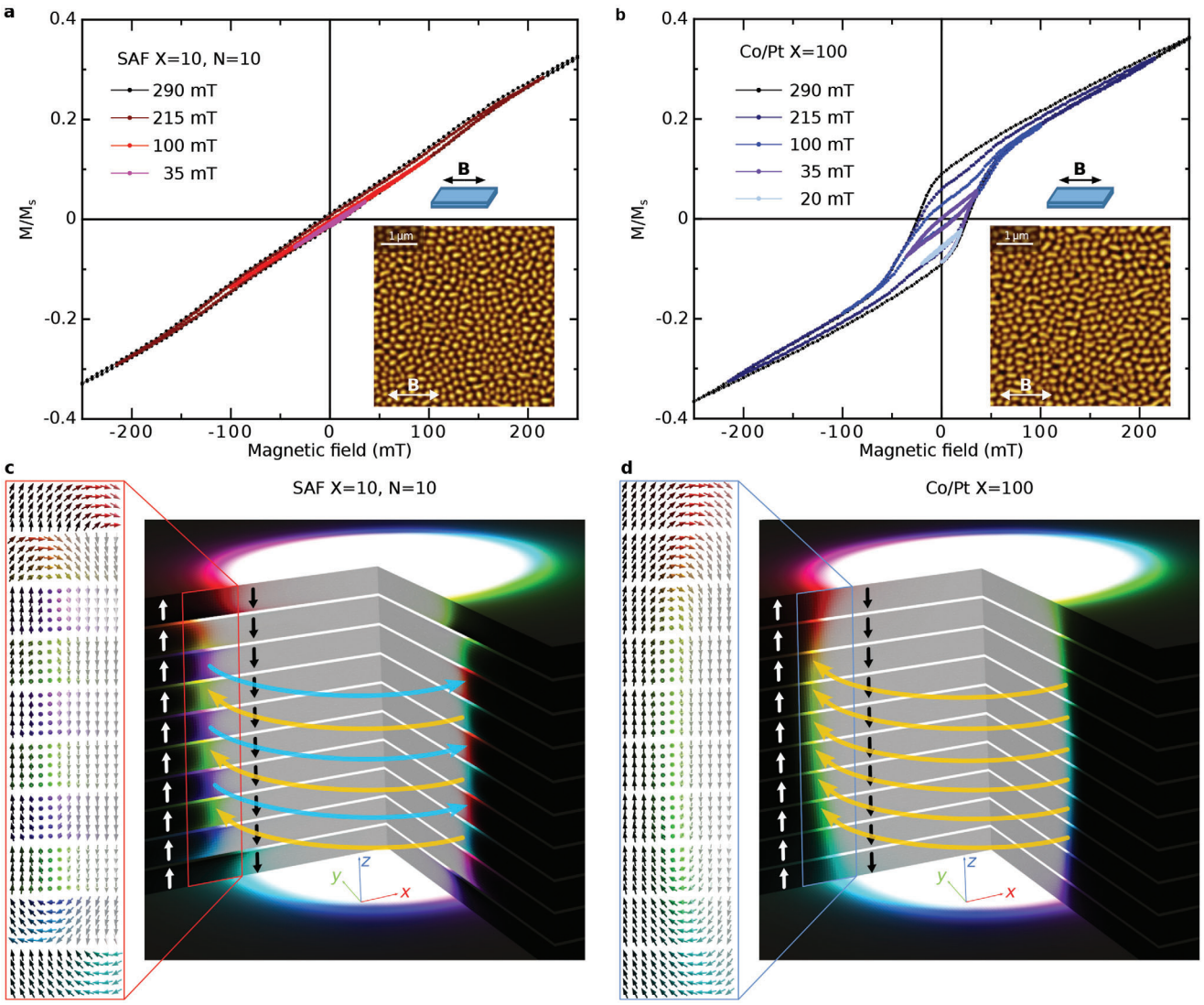

Figure 4. Bubble domains in PMA-SAFs and PMA-FM. a,b) Magnetic minor hysteresis loop series with the maximum magnetic field varied between 20 and 290 mT, for a PMA-SAF $[[Co(0.44\ nm)/Pt(0.7\ nm)]_9/Co(0.44\ nm)/Ru(0.9\ nm)]_9[Co(0.44\ nm)/Pt(0.7\ nm)]_{10}$ ML (a) and a PMA-FM $[Co(0.44\ nm)/Pt(0.7\ nm)]_{100}$ ML (b) system in bubble-domain states. The field is applied parallel to the film plane. Insets represent corresponding bubble-domain states recorded using MFM. c,d) The result of micromagnetic simulations for the bubble domains in the SAF (c) and FM (d) MLs at perpendicular magnetic field of 300 mT. The white and black arrows represent the "up" and "down" domain polarization. The spin structure in the corresponding domain walls is color-coded as shown in the zoomed views in the left panels of (c) and (d).

perpendicular stripe and bubble domains separated by AF Bloch-type DWs. This domain wall structure offers unique possibilities for a wide range of functionalities in PMA-SAFs. One promising avenue lies in integrating 3D memory and logic[54] with the skyrmion race track memory concept.[2,3,23] **Figure 5** illustrates this concept, where each individual bubble domain on a track encodes data through the sequence of the chirality of the domain walls in the FM stacks. Since the magnetic configuration near the surface (Néel caps) always follows the demagnetizing fields, the endmost FM stacks remain identical for all configurations and are not involved in the data encoding scheme. The number of possible states encoded in each magnetic bubble depends on the number of ferromagnetic stacks in the ML and equals 2^{N_s}, where N_s is the number of FM stacks in the ML except those two at the top and bottom hosting Néel caps.

For weak AF or FM IEC, either bubbles denoted as state I (and IV) or state II in Figure 5 are stable, respectively. However, as demonstrated in a recent study,[33] when the interlayer exchange coupling tends to zero, states with different DW chirality sequences become energetically equivalent. Recent studies have also shown that multilayers with IEC can be reversibly switched between FM and AF states via voltage gating,[55,56] enabling the potential for electrical manipulation of the DW state.

This information encoding approach, combined with the controlled movement of bubbles along nanotracks, can contribute to the concept of multidimensional logic.[42,54] The identical size,

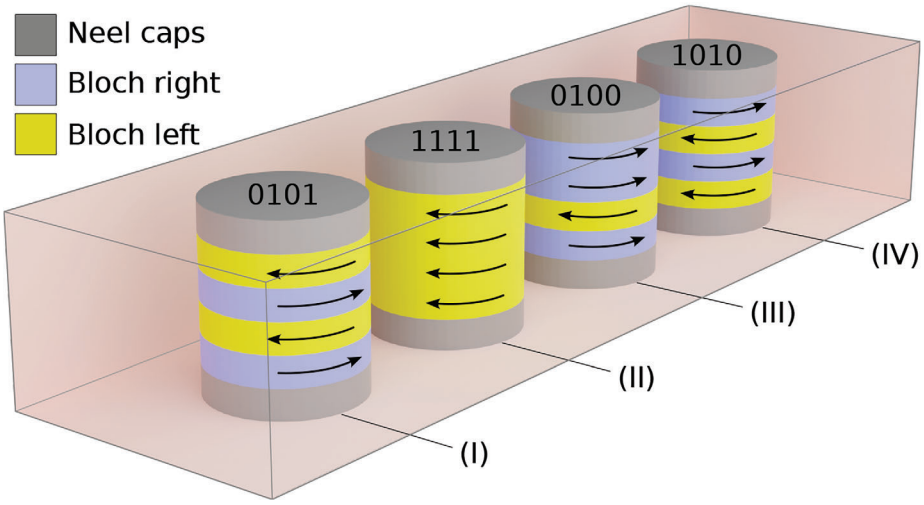

Figure 5. Data encoding concept using alternating chirality of the domain walls in bubble domains. When the IEC between Co/Pt blocks approaches zero, bubble domains with varying sequences of right-handed (0) and left-handed (1) chirality in the DWs can coexist[33]. These domains have nearly identical sizes and energies. The endmost blocks, which includes Néel caps, cannot be switched. In the case of four switchable blocks, there are 16 possible configurations (a four-bit word per bubble), with only four illustrated in the figure.

axial symmetry, and topological properties of these magnetic bubbles suggest that they will respond identically to external stimuli, ensuring synchronous motion along the track. However, the practical realization of such a concept requires addressing several challenges, including the controllable switching between the states depicted in Figure 5 and the electrical detection of specific states.

Additionally, the AF DWs inherent in aligned stripe domains provide a pathway for guiding spin waves with nonreciprocal propagation characteristics.[34–37] Overall, our findings extend the perspective for domain wall structure design and unveil a previously unexplored pathway towards integrating FM order in nanoscale size domains with AF order in Bloch-type DWs between them.

4. Experimental Section

Sample Fabrication: The MLs were fabricated using dc magnetron sputter deposition at 3×10^{-3} mbar Ar atmosphere in an ultrahigh vacuum ATC 2200 system from AJA International Inc. Si wafers with 100-nm-thick thermally oxidized (SiO_2) layer as well as Si_3N_4 membranes were used as substrates. Prior to the ML deposition, a 1.5 nm Ta layer was deposited for adhesion purposes. A subsequent Pt layer (20 nm on SiO_2 and 5 nm on Si_3N_4) served as a seed in order to obtain a preferred Co/Pt (0001)/(111)-texture, which supports better growth and larger PMA.[57] The samples were finally capped by a 2 nm Pt layer to avoid surface oxidation. All metallic layers were deposited at room temperature utilizing alternating source shutters. To ensure uniform growth of the entire stack, the sample holder was set in rotation at ≈60 rpm. The Co, Ru, and Ta target guns were positioned at an angle of 30° in relation to the substrate's normal, while Pt layers were deposited in a face-to-face configuration. The thickness of each layer was controlled via deposition time. Prior to fabricating the samples, the sputter rates (0.07 nm s^{-1} for Co at 80 W dc power; 0.12 nms^{-1} for Pt at 40 W; and 0.04 nm s^{-1} for Ru at 50 W) were calibrated using X-ray reflectivity.

Characterizations and Measurements: Structural characterization of the sample architecture was performed via X-ray reflectivity using a Cu K_α radiation source diffractometer (Rigaku SmartLab XG). Exemplary reflectivity profiles are displayed for the (X, N) = (10, 10) SAF versus X = 100 Co/Pt sample in Figure S1 (Supporting Information) and allow a clear distinction between the double period ML SAF versus the single period Co/Pt ML.

Magnetic measurements were performed using a commercial Microsense EZ7 vibrating sample magnetometer (VSM), equipped with an electromagnet, which delivers up to 1.8 T magnetic field. The saturation magnetization of all samples was measured using the VSM and calculated to be $M_s = 0.8 \pm 0.1$ MA m^{-1} for both SAF and Co/Pt systems. The PMA constant was determined from the in-plane saturation field of a Co/Pt sample with $X = 12$. Accordingly, by varying the Co thickness and keeping the Pt thickness constant (0.7 nm) the largest PMA was obtained within the sample set to be of ≈0.6 MJ m^{-3} at the Co thickness of 0.44 nm.

The AF exchange constant in SAFs was derived from the calibration $\{[Co(0.44\ nm)/Pt(0.7\ nm)]_{X-1}/Co(0.44\ nm)/Ru(0.9\ nm)\}_{N-1}[Co(0.44\ nm)/Pt(0.7\ nm)]_X$ ML with (X, N) = (5, 2), which shows a rectangular shape of the field-dependent magnetization in the out-of-plane geometry (see Figure S6, Supporting Information). The interlayer exchange coupling constant $J_{iec} \approx -1$ mJ m^{-2} was calculated according to the equation $J_{iec} = -M_s d_{Co/Pt} B$, where $d_{Co/Pt}$ is the thickness of a Co/Pt $X = 5$ block, and B is the averaged spin-flip field. Having all parameters (M_s, PMA, and J_{iec}) for SAF MLs fixed, the X and N were varied until the FM state in SAFs was reached according to the diagram in Ref. [28].

The aligned stripe domain states in all the samples were prepared using a specific ac-demagnetization (ACD) routine, namely by alternating the magnetic field direction parallel to the sample surface with subsequent reduction of the field amplitude from 1.8 T down to 2 mT in 2% steps.

Imaging Techniques: Magnetic domain imaging was performed using a Bruker Dimension Icon atomic force microscope. The LTEM studies were performed with a JEOL Jem F-200C - transmission electron microscope, operated at 200 kV acceleration voltage, in the Lorentz (Fresnel) mode. All images were recorded at room temperature.

Micromagnetic Simulations: The total micromagnetic energy of the system included the following terms: Heisenberg exchange, interlayer

exchange coupling, uniaxial anisotropy, Zeeman energy, and the energy of the demagnetizing fields. In a multilayer system, the exchange coupling between Co layers across the Pt inter-layer is weaker than the direct exchange within the Co layer. It was assumed that the plane of the multilayer is in the *xy*-plane. Thereby the Heisenberg exchange interaction energy density within the Co/Pt stack can be approximated as follows[32]

$$w_{ex} = A \sum_i \left[\left(\frac{\partial m_i}{\partial x} \right)^2 + \left(\frac{\partial m_i}{\partial y} \right)^2 + k_{iec} \left(\frac{\partial m_i}{\partial z} \right)^2 \right] \quad (1)$$

where the summation runs over $i = x, y, z$ components of the magnetization unit vector field, $\mathbf{m} = \mathbf{M}/M_s$. The constant A is the exchange stiffness in the plane of the film, while the unitless constant k_{iec} defines the strength of the exchange coupling between Co layers across the Pt layers. In these simulations, $A = 8$ pJ m^{-1} and $k_{iec} = 0.2$ estimated for $[(\mathrm{Co}(0.44\ \mathrm{nm})/\mathrm{Pt}(0.7\ \mathrm{nm})]_X$ multilayers in Ref. [32] were used.

The interlayer exchange coupling of Co/Pt stacks across Ru interlayer was defined by the following surface energy density expression:

$$w_{iec} = -J_{iec}(\mathbf{m}_1 \cdot \mathbf{m}_2) \quad (2)$$

where $\mathbf{m}_1$ and $\mathbf{m}_2$ are the magnetization at the interfaces (Co/Ru interface and Ru/Co interface), and J_{iec} is the coupling constant given in units of J m^{-2}. For ferromagnetic interlayer exchange coupling, $J_{iec} > 0$ and for antiferromagnetic coupling $J_{iec} < 0$. In practice, on a discrete lattice of cuboids, the energy term (2) was implemented as follows,

$$w_{iec} = -J_{iec} \frac{\mathbf{m}_i \cdot \mathbf{m}_j}{\Delta_z} \quad (3)$$

where $\mathbf{m}_i$ and $\mathbf{m}_j$ are the magnetization in the cuboids separated by the nonmagnetic spacer as illustrated in Figure S7c (Supporting information), and Δ_z is the height of the cuboids along the *z*-axis. To implement this interaction in Mumax, the option of custom effective fields was used. For details of implementation, see the Mumax script files in Supporting Information. In these simulations, the experimentally estimated value of antiferromagnetic interlayer exchange coupling $J_{iec} = -1$mJ m^{-2} corresponding to a 0.9-nm-thick Ru layer was implemented. Furthermore, the experimentally measured values of saturation magnetization $M_s \sim = \sim 775$ kA m^{-1} and uniaxial anisotropy $K_u \sim = \sim 0.6$ MJ m^{-3} were used. For the calculation of the isolated stripe domain and equilibrium period of stripe domains at zero applied magnetic fields (see Figure S7d, Supporting Information) in the $X = 12$, $N = 4$ multilayer, a mesh density of $256 \times 256 \times 51$ cuboids was employed. The thickness of the cuboids along the *z*-axis was set to 1 nm, while the lateral size of the cuboid may vary in the range between 1 and 2 nm. The data presented in this figure could be reproduced with the Mumax script in Supplementary Software 1.

For the simulation presented in Figure 1e,f, a domain of square shape in the *xy*-plane with a size of $L_x = L_y = 320$ nm (twice the stripe-domain period) was implemented, while for simulations in Figure 2, a domain with $L_x = L_y = 512$ nm was used.

To simulate the bubble domains shown in Figure 4c,d, a square domain with $L_x = L_y = 256$ nm was employed and a perpendicular magnetic field of 300 mT was applied. These simulations could be reproduced with the Mumax script in Supplementary Software 2. As an additional verification, the results of micromagnetic simulations in Mumax were double-checked using the Excalibur code.[47] Additionally, Excalibur was used to calculate Lorentz TEM images, as discussed in the following section.

Simulations of Lorentz TEM Images: To calculate the Lorentz TEM images in the case of an electron beam perpendicular to the film plane, a well-established approach based on phase object approximation was followed,[58] in detail described in Ref. [59]. When the electron beam has an arbitrary tilt angle to the plane of the sample, the magnetic contribution to the phase shift can be calculated as:[60]

$$\varphi(x', y') = \frac{2\pi e}{h} \int_{-\infty}^{+\infty} dz\, \mathbf{A}_d \cdot \mathbf{n}_e \quad (4)$$

where $\mathbf{n}_e$ is the unit vector along the incident electron beam, e is an elementary (positive) charge and h is Planck's constant, $\mathbf{A}_d$ is the magnetic vector potential induced by the sample magnetization, and x' and y' are the coordinates in the plane orthogonal to the beam direction. The theoretical LTEM images, presented in Figure 2, were calculated with the Excalibur code.

Supporting Information

Supporting Information is available from the Wiley Online Library or from the author.

Acknowledgements

The authors are grateful to Thomas Naumann and Jakob Heinze for experimental and technical support. N.S.K. thanks Filipp Rybakov for the fruitful discussions and for providing access to the Excalibur code. This work was supported by the Deutsche Forschungsgemeinschaft through project 514946929 (Gemischt-ferromagnetisch-antiferromagnetische Hybridphase von Streifen- und "Bubble"-Domänenstrukturen für magnonische Kristall und "Race-Track"-Anwendungen) and within the priority program SPP 2137 through project 403503416. N.S.K. acknowledges the support from the European Research Council (ERC) under the European Union's Horizon 2020 research and innovation program (Grant No. 856538, project "3D MAGiC"). S.S. acknowledges the support from the Deutsche Forschungsgemeinschaft through project 458685885.

Conflict of Interest

The authors declare no conflict of interest.

Data Availability Statement

The Mumax scripts used for micromagnetic simulations can be found in the repository at https://zenodo.org/doi/10.5281/zenodo.11204376.

Keywords

alternating chirality, bubble domains, domain walls, magnetic solitons, synthetic antiferromagnets

Received: April 5, 2024
Published online: May 13, 2024

[1] S. Woo, K. Litzius, B. Krüger, M.-Y. Im, L. Caretta, K. Richter, M. Mann, A. Krone, R. M. Reeve, M. Weigand, P. Agrawal, I. Lemesh, M.-A. Mawass, P. Fischer, M. Kläui, G. S. D. Beach, *Nat. Mater.* **2016**, *15*, 501.
[2] A. Fert, N. Reyren, V. Cros, *Nat. Rev. Mater.* **2017**, *2*, 17031.
[3] N. Nagaosa, Z. Tokura, *Nat. Nanotechnol.* **2013**, *8*, 899.
[4] R. Tomasello, E. Martinez, R. Zivieri, L. Torres, M. Carpentieri, G. Finocchio, *Sci. Rep.* **2014**, *4*, 6784.

[5] W. Jiang, X. Zhang, G. Yu, W. Zhang, X. Wang, M. B. Jungfleisch, J. E. Pearson, X. Cheng, O. Heinonen, K. L. Wang, Y. Zhou, A. Hoffmann, S. G. E. Velthuis, *Nat. Phys.* **2017**, *13*, 162.
[6] K. Litzius, I. Lemesh, B. Krüger, P. Bassirian, L. Caretta, K. Richter, F. Büttner, K. Sato, O. A. Tretiakov, J. Förster, R. M. Reeve, M. Weigand, I. Bykova, H. Stoll, G. Schütz, G. S. D. Beach, M. Kläui, *Nat. Phys.* **2017**, *13*, 170.
[7] W. Legrand, J.-Y. Chauleau, D. Maccariello, N. Reyren, S. Collin, K. Bouzehouane, N. Jaouen, V. Cros, A. Fert, *Sci. Adv.* **2018**, *4*, eaat0415.
[8] J. Lucassen, M. J. Meijer, O. Kurnosikov, H. J. M. Swagten, B. Koopmans, R. Lavrijsen, F. K.-Twesten, R. Frömter, R. A. Duine, *Phys. Rev. Lett.* **2019**, *123*, 157201.
[9] M. J. Meijer, J. Lucassen, F. Kloodt-Twesten, R. Frömter, O. Kurnosikov, R. A. Duine, H. J. M. Swagten, B. Koopmans, R. Lavrijsen, *Phys. Rev. Lett.* **2020**, *124*, 207203.
[10] A. P. Malozemoff, J. C. Slonczewski, *Magnetic Domain Walls in Bubble Materials*, Academic Press, New York **1979**.
[11] A. Hubert, R. Schäfer, *Magnetic Domains*, Springer, Berlin **2009**.
[12] C. Moreau-Luchaire, C. Moutafis, N. Reyren, J. Sampaio, C. A. F. Vaz, N. Van Horne, K. Bouzehouane, K. Garcia, C. Deranlot, P. Warnicke, P. Wohlhüter, J.-M. George, M. Weigand, J. Raabe, V. Cros, A. Fert, *Nat. Nanotechnol.* **2016**, *11*, 444.
[13] S. D. Pollard, J. A. Garlow, J. Yu, Z. Wang, Y. Zhu, H. Yang, *Nat. Commun.* **2017**, *8*, 14761.
[14] S. S. P. Parkin, N. More, K. P. Roche, *Phys. Rev. Lett.* **1990**, *64*, 2304.
[15] M. D. Stiles, *J. Magn. Magn. Mater.* **1999**, *200*, 322.
[16] S.-H. Yang, K.-S. Ryu, S. Parkin, *Nat. Nanotechnol.* **2015**, *10*, 221.
[17] T. Dohi, S. DuttaGupta, S. Fukami, H. Ohno, *Nat. Commun.* **2019**, *10*, 5153.
[18] W. Legrand, D. Maccariello, F. Ajejas, S. Collin, A. Vecchiola, K. Bouzehouane, N. Reyren, V. Cros, A. Fert, *Nat. Mater.* **2020**, *19*, 34.
[19] R. Chen, Y. Gao, X. Zhang, R. Zhang, S. Yin, X. Chen, X. Zhou, Y. Zhou, J. Xia, Y. Zhou, S. Wang, F. Pan, Y. Zhang, C. Song, *Nano Lett.* **2020**, *20*, 3299.
[20] R. Juge, N. Sisodia, J. U. Larrañaga, Q. Zhang, V. T. Pham, K. G. Rana, B. Sarpi, N. Mille, S. Stanescu, R. Belkhou, M.-A. Mawass, N. Novakovic-Marinkovic, F. Kronast, M. Weigand, J. Gräfe, S. Wintz, S. Finizio, J. Raabe, L. Aballe, M. Foerster, M. Belmeguenai, L. D. Buda-Prejbeanu, J. Pelloux-Prayer, J. M. Shaw, H. T. Nembach, L. Ranno, G. Gaudin, O. Boulle, *Nat. Commun.* **2022**, *13*, 4807.
[21] R. Chen, Q. Cui, L. Han, X. Xue, J. Liang, H. Bai, Y. Zhou, F. Pan, H. Yang, C. Song, *Adv. Funct. Mater.* **2022**, *32*, 2111906.
[22] R. A. Duine, K.-J. Lee, S. S. P. Parkin, M. D. Stiles, *Nat. Phys.* **2018**, *14*, 217.
[23] M. Fattouhi, K. Y. Mak, Y. Zhou, X. Zhang, X. Liu, M. E. Hafidi, *Phys. Rev. Appl.* **2021**, *16*, 014040.
[24] K. M. Song, J.-S. Jeong, B. Pan, X. Zhang, J. Xia, S. Cha, T.-E. Park, K. Kim, S. Finizio, J. Raabe, J. Chang, Y. Zhou, W. Zhao, W. Kang, H. Ju, S. Woo, *Nat. Electron.* **2020**, *3*, 148.
[25] K. Wang, V. Bheemarasetty, G. Xiao, *APL Mater.* **2023**, *11*, 070902.
[26] O. Hellwig, T. L. Kirk, J. B. Kortright, A. Berger, E. E. Fullerton, *Nat. Mater.* **2003**, *2*, 112.
[27] O. Hellwig, A. Berger, E. E. Fullerton, *Phys. Rev. Lett.* **2003**, *91*, 197203.
[28] O. Hellwig, A. Berger, J. B. Kortright, E. E. Fullerton, *J. Magn. Magn. Mater.* **2007**, *319*, 13.
[29] C. Bran, A. B. Butenko, N. S. Kiselev, U. Wolff, L. Schultz, O. Hellwig, U. K. Rößler, A. N. Bogdanov, V. Neu, *Phys. Rev. B* **2009**, *79*, 024430.
[30] T. Hauet, C. M. Günther, O. Havorka, A. Berger, M.-Y. Im, P. Fischer, T. Eimüller, O. Hellwig, *Appl. Phys. Lett.* **2008**, *93*, 042505.
[31] O. Hellwig, C. M. Günther, F. Radu, A. Menzel, W. F. Schlotter, J. Lüning, S. Eisebitt, *Appl. Phys. Lett.* **2011**, *98*, 172503.
[32] R. Salikhov, F. Samad, B. Böhm, S. Schneider, D. Pohl, B. Rellinghaus, A. Ullrich, M. Albrecht, J. Lindner, N. S. Kiselev, O. Hellwig, *Phys. Rev. Appl.* **2021**, *16*, 034016.
[33] A. S. Savchenko, V. M. Kuchkin, F. N. Rybakov, N. S. Kiselev, *Front. Phys.* **2023**, *11*, 1223609.
[34] C. Banerjee, P. Gruszecki, J. M. Klos, O. Hellwig, M. Krawczyk, A. Barman, *Phys. Rev. B* **2017**, *96*, 024421.
[35] P. Gruszecki, C. Banerjee, M. Mruczkiewicz, O. Hellwig, A. Barman, M. Krawczyk, *Solid State Phys.* **2019**, *70*, 79.
[36] D. Petti, S. Tacchi, E. Albisetti, *J. Phys. D: Appl. Phys.* **2022**, *55*, 293003.
[37] L. Qiu, K. Shen, *Phys. Rev. B* **2022**, *105*, 094436.
[38] S. Li, W. Kang, Y. Huang, X. Zhang, Y. Zhou, W. Zhao, *Nanotechnology* **2017**, *283*, 1LT01.
[39] G. Bourianoff, D. Pinna, M. Sitte, K. Everschor-Sitte, *AIP Adv.* **2018**, *8*, 055602.
[40] A. Kurenkov, S. Fukami, H. Ohno, *J. Appl. Phys.* **2020**, *128*, 010902.
[41] J. Grollier, D. Querlioz, K. Y. Camsari, K. Everschor-Sitte, S. Fukami, M. D. Stiles, *Nat. Electron.* **2020**, *3*, 360.
[42] S. Li, W. Kang, X. Zhang, T. Nie, Y. Zhou, K. L. Wang, W. Zhao, *Mater. Horiz.* **2021**, *8*, 854.
[43] S. J. Yun, S. H. Sang Ho Lim, S.-R. Lee, *AIP Adv.* **2016**, *6*, 025112.
[44] R. C. Carvalho, I. P. Miranda, J. Brandão, A. Berman, J. C. Cezar, A. B. Klautau, H. M. Petrilli, *Nano Lett.* **2023**, *23*, 4854.
[45] W. Legrand, Y. Sassi, F. Ajejas, S. Collin, L. Bocher, H. Jia, M. Hoffmann, B. Zimmermann, S. Blügel, N. Reyren, V. Cros, A. Thiaville, *Phys. Rev. Mater.* **2022**, *6*, 024408.
[46] A. Vansteenkiste, J. Leliaert, M. Dvornik, M. Helsen, F. Garcia-Sanchez, B. Van Waeyenberge, *AIP Adv.* **2014**, *4*, 10.
[47] F. N. Rybakov, E. Babaev, *Excalibur software*, http://quantumandclassical.com/excalibur/.
[48] M. Ohring, *The Material Science of Thin Films*, Academic Press, New York **1992**.
[49] R. Salikhov, F. Samad, S. S. P. K. Arekapudi, R. Ehrler, J. Lindner, N. S. Kiselev, O. Hellwig, *Phys. Rev. B* **2022**, *106*, 054404.
[50] P. Dekker, J. C. Slonczewski, *Appl. Phys. Lett.* **1976**, *29*, 753.
[51] K. Patek, R. Gemperle, L. Murtinova, J. Kaczer, *J. Magn. Magn. Mater.* **1993**, *123*, 223.
[52] N. S. Kiselev, I. E. Dragunov, U. K. Rößler, A. N. Bogdanov, *Appl. Phys. Lett.* **2007**, *91*, 132507.
[53] N. S. Kiselev, U. K. Rößler, A. N. Bogdanov, O. Hellwig, *Appl. Phys. Lett.* **2008**, *93*, 162502.
[54] R. Lavrijsen, J.-H. Lee, A. Fernandez-Pacheko, D. C. M. C. Petit, R. Mansell, R. P. Cowburn, *Nature* **2013**, *493*, 647.
[55] A. E. Kossak, M. Huang, P. Reddy, D. Wolf, G. S. D. Beach, *Sci. Adv.* **2023**, *9*, 054.
[56] M. Ameziane, R. Rosenkamp, L. Flajšman, S. van Dijken, R. Mansell, *Appl. Phys. Lett.* **2023**, *122*, 232401.
[57] L. Fallarino, A. Oelschlägel, J. A. Arregi, A. Bashkatov, F. Samad, B. Böhm, K. Chesnel, O. Hellwig, *Phys. Rev. B* **2019**, *99*, 024431.
[58] M. De Graef, In: Experimental Methods in the Physical Sciences **2001**, *36*, 27.
[59] F. Zheng, F. N. Rybakov, N. S. Kiselev, D. Song, A. Kovacs, H. Du, S. Blügel, R. E. Dunin-Borkowski, *Nat. Commun.* **2021**, *12*, 5316.
[60] H. Lichte, M. Lehmann, *Rep. Prog. Phys.* **2008**, *70*, 016102.